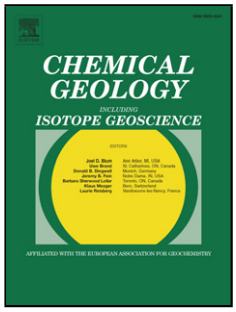

Constraining *in situ* cosmogenic nuclide paleo-production rates using sequential lava flows during a paleomagnetic field strength low

A.M. Balbas, K.A. Farley

PII: S0009-2541(19)30484-X

DOI: https://doi.org/10.1016/j.chemgeo.2019.119355

Reference: CHEMGE 119355

To appear in:

Received Date: 6 August 2019

Revised Date: 26 September 2019

Accepted Date: 31 October 2019

Please cite this article as: Balbas AM, Farley KA, Constraining *in situ* cosmogenic nuclide paleo-production rates using sequential lava flows during a paleomagnetic field strength low, *Chemical Geology* (2019), doi: https://doi.org/10.1016/j.chemgeo.2019.119355

Constraining *in situ* cosmogenic nuclide paleo-production rates using sequential lava flows during a paleomagnetic field strength low

A.M. Balbas[1,2]*, K.A. Farley[2]

[1] College of Earth, Ocean, and Atmospheric Sciences, Oregon State University, Corvallis, OR, USA

[2]Department of Geological and Planetary Sciences, California Institute of Technology, Pasadena, CA, USA

* Corresponding author: Andrea.Balbas@oregonstate.edu

Abstract

The geomagnetic field prevents a portion of incoming cosmic rays from reaching Earth's atmosphere. During magnetic reversals and excursions, the field strength can decrease by up to 90% relative to the modern-day value. During such anomalies, cosmic ray bombardment to Earth's atmosphere increases as evident from atmospheric ^{10}Be anomalies recorded in sediment and ice cores. However, how the flux of cosmic rays to Earth's surface varies during such geomagnetic anomalies is not well constrained. We measured fossil cosmogenic ^{3}He in olivine from the tops of two pairs of ^{40}Ar/^{39}Ar age-dated Tahitian lava flows that erupted during the Matuyama-Brunhes reversal precursor event. We corrected these raw values for the diffusive loss of helium caused by heating from the overlying flow with a diffusion model using cooling rates and maximum temperature conditions based on field measurements of active lava flows from Kilauea, Hawaii. We assume the maximum temperature suggested by field measurements and thus present a limiting case for the highest diffusive loss corrections and thus the highest paleo-production rates. Based on paleomagnetic field strength reconstructions and scaling factor models, the upper limits of

the corrected *in situ* ^{3}He paleo-production rates (100 ± 23, 144 ± 35 atoms g^{-1} a^{-1}) are in agreement with those expected during the period of a geomagnetic field strength low when these flow tops were exposed. However, the more plausible contact temperatures (<700ºC maximum temperature in diffusion model) are associated with diffusion corrected paleo-production rates lower than those predicted by scalar models. This potential underestimation is likely a function of changes in local non-dipole field components, atmospheric density and/or an overestimation of the dipole field strength reduction during the M-B precursor event.

Keywords: Cosmogenic Nuclides; Paleomagnetism; Matuyama-Bruhnes; Magnetic Reversal; Helium-3; production rates; cosmic rays

Introduction:

Earth's magnetic field shields the planet and its biosphere from high energy galactic and solar cosmic rays (Elsasser et al., 1956; Mead, 1964). However, the character of Earth's magnetic field changes during excursions and polarity reversals (Gubbins, 1999; Jarboe et al., 2011; McElhinny and McFadden, 1998; McFadden et al., 1991). During these anomalies the geomagnetic field decreases in intensity, changes in orientation and reveals non-dipole components (Coe and Glen, 2004; Jarboe et al., 2011; Valet and Plenier, 2008).

Particles with enough energy to pass through Earth's magnetic field (primary particles) bombard the atmosphere producing a cascade of secondary particles including protons and

neutrons. Secondary particles (largely neutrons) interact with atoms in surface minerals producing *in situ* cosmogenic nuclides, such as ^{3}He (Gosse and Phillips, 2001). The relationship between Earth's magnetic field and the production rate of atmospheric cosmogenic nuclides is fairly well-constrained over the past ~50 kyr (Menabreaz et al., 2012; Muscheler et al., 2005; Raisbeck et al., 1981). Atmospheric cosmogenic nuclide production rates show a distinct increase during the Laschamp excursion field strength low (Leduc et al., 2006; McHargue et al., 1995; Ménabréaz et al., 2011). Records from ice and sediment cores during the field strength low associated with the Matuyama-Brunhes (M-B) reversal also show an increased production rate of atmospheric ^{10}Be (Raisbeck et al., 2006; Simon et al., 2017; Suganuma et al., 2010) (**Figure 1**). However, no observations exist regarding the flux of secondary particles reaching Earth's surface and the resulting change in *in situ* cosmogenic nuclide paleo-production rates during paleomagnetic anomalies.

Here we report *in situ* paleo-production rates of spallogenic ^{3}He during a field strength low associated with the M-B reversal precursor event. First, we independently define the time a lava flow was exposed to cosmic rays by calculating the age difference between sequential overlapping flows. By subtracting the high-precision ^{40}Ar/^{39}Ar age of the overlying flow from the underlying flow, a surface exposure time is calculated. Next, ^{3}He is measured in olivine grains that are separated from the top 4 cm of the underlying flow. Then we corrected for the diffusive loss of He due to heating from the overlying flow using the He in olivine diffusion parameters from Blard et al. (2008). Finally, we compared the modeled paleo-production rates with modern-day production rates for this site. The modeled paleo-production rates range from those expected during the magnetic field strength low associated with the precursor event and modern-day production rate values at this location.

Geologic Setting:

This experiment required a field site comprised of lava flows that were formed during a paleomagnetic field strength low associated with a known polarity reversal and field strength reduction. Olivine-bearing alkali basalts are ideal for this study because they contain both olivine for cosmogenic ^{3}He measurements and enough potassium to yield high-precision $^{40}Ar/^{39}Ar$ age determinations. Field sites from the low latitudes are preferred because this region is likely to experience the largest relative change in production rates associated with geomagnetic field strength changes. This is because Earth's magnetic field lines are generally parallel to the planet's surface in the low latitudes and thus more effective at repelling charged particles when the field is at full strength (Elsasser et al., 1956). Lastly, our experiment requires consecutive overlain lava flows formed during a paleomagnetic field strength low.

A series of lava flows in the Punaruu valley of Tahiti-Nui meet all of the above criteria (Balbas et al., 2018; Mochizuki et al., 2011). The polarity orientation of these flows ranges through normal, reversed, and transitional, and record field intensity as low as ~5 μT during the time of formation (Mochizuki et al., 2011). This represents a field strength reduction of up to ~86% compared to modern-day (Thébault et al., 2015). The flows vary in age from 771 to 805 ka and cover both the precursor and transitional phases of the M-B polarity reversal (Balbas et al., 2018). This study focuses on hand-samples taken from four lava flows that span ~20 m horizontally and >6 m vertically (Balbas et al., 2018; Mochizuki et al., 2011). The series of flows are located at 186 m elevation and the contacts between flows are clear with no discernable erosion or ash beds (**Figure 2**). Paleosol layers were not observed or expected given the slow rate of soil development on basaltic lava flows (~0.3 m/Ma) (Pillans, 1997). The thickness of overlying flows (~4 m) was sufficient to ensure no significant post-burial production of ^{3}He. This sequence was exposed in

road cuts during the 1990's implying negligible contributions from modern exposure. Flows are clinopyroxene and olivine bearing alkali basalts with cryptocrystalline to holocrystalline groundmass matrices.

This study focuses on contacts between lava flows B1-B2 and B3-B4 (Balbas et al., 2018; Mochizuki et al., 2011). Flow B1 was exposed during a field strength low shown in the PISO1500 (Channell et al., 2009) and PADM2M (Ziegler et al., 2011) paleo-intensity stacks (**Figure 1**) at ~800-790 ka. Flow B3 formed during a time of slight field strength recovery (790-780 ka), prior to the final reversal phase (**Figure 1**). Both lava flows would have been exposed to surface radiation during a time-interval of reduced paleomagnetic field intensity known as the M-B precursor event (Channell et al., 2009; Hartl and Tauxe, 1996; Raisbeck et al., 2006; Singer et al., 2005). Flow B1 has an $^{40}Ar/^{39}Ar$ age of 801.7 ± 2.9 ka (2σ; n=6) and B3 has an age of 792.2 ± 4.8 ka (n=4) (Balbas et al., 2018). The overlying flows B2 and B4 have ages of 793.7 ± 4.1 (n=5) and 781.3 ± 3.9 ka (n=4) respectively (Balbas et al., 2018). The resulting exposure times for B1-B2 is 8.0 ± 5.0 ka and B3-B4 is 10.9 ± 6.2 ka.

The modern-day production rate for ^{3}He in olivine at our field site is 76 ± 12 (2σ) atoms*g^{-1}*a^{-1}, which is calculated using the ^{3}He production rates in olivine from Goehring et al. (2010) (120 ± 18.8, 2σ, at sea level and high latitude) and a latitude-elevation-field strength production rate scaling factor of 0.63 which is calculated using the LSD model of Lifton et al. (2014) and includes corrections for the dip of the flow and topographic shielding. If continual subsidence of Tahiti-Nui is assumed to have occurred over the past 790 kyrs then the lava flows would have been emplaced at a higher elevation. Subsidence rates of Tahiti are reported at -0.05 (± 2.0) mm/yr (Fadil et al., 2011). If considered at this value, the total subsidence would be 40 m resulting in a 3% increase of the scalar-derived paleo-production rate. However, due to the large uncertainty of

the subsidence rate, we have chosen not to include this increase in the LSD modeled paleo-production rates. During the M-B precursor event the production rate at this site is assumed to increase due to the decreased strength of the magnetic field. The increased production rate can be calculated using the LSD scalar model (Lifton et al., 2014), which uses the magnetic field paleo-intensity stack PADM2M (Ziegler et al., 2011). This stack includes multiple records of the field intensity low of the precursor event, and thus the scaling factor for samples exposed at this time is larger than during modern day. The mean modeled scalar value for the time period when these two flow tops were exposed is 1.03, which corresponds to a ^{3}He production rate of 124 ± 19 atoms*g^{-1}*a^{-1} for our field site location during the precursor event. The uncertainty includes the production rate uncertainty from Goehring et al. (2010). It is important to note, these uncertainties only include the error on the ^{3}He production rate (15.7%; 2σ) and do not include errors associated with the scalar or paleomagnetic field strength reconstructions used in the scalar as it has been argued that it is not possible to make uniform assessments of the inherent errors in scaling production rates (Desilets et al., 2006).

Methods:

To ensure samples contained fossil cosmogenic ^{3}He, bulk samples were taken from sections that had the clearest identifiable contacts between pairs of consecutive flows (**Figure 2**). The top 4 cm of the underlying flow, directly below the contact, were collected to produce olivine mineral separates for ^{3}He analysis.

The ^{3}He in olivine phenocrysts can come from both cosmogenic and magmatic sources. To isolate the cosmogenic component we used the methods outlined in Kurz (1986). This method involves crushing olivine grains *in vacuo* to determine the inherited (atmospheric and magmatic) ^{3}He/^{4}He held within inclusions and grain defects. To obtain the inherited ^{3}He concentration of the

lava flows, ~200 mg of olivine (0.5 – 1 mm size fraction) was separated from samples collected from the core of the lava flow (shielded at ~0.5- 1.0 m from the paleosurface). These separates were loaded into stainless steel crushers and crushed *in vacuo* at the Oregon State University laboratory following procedures outlined in Konrad et al. (2018).

Fusion analyses of the surface-exposed samples were carried out in the noble gas laboratory at Caltech. Olivine grains (150 - 500 µm) were hand-picked under a binocular microscope in order to provide a homogenous separate with minimal alteration. The olivine separates were crushed to a fine powder (<40 µm) under ethanol to release any magmatic helium in fluid inclusions while avoiding absorption of atmospheric He into the grains (Cox et al., 2017; Protin et al., 2016). Between 302 and 984 mg of crushed olivine were loaded into a high temperature furnace and brought under vacuum. Separates were heated to ~1300^{o}C for 15 minutes, prior to being inlet into a gas processing line. Released gases were sequentially exposed to two SAES NP10 getters kept at 250^{o}C and room temperature, respectively. Purified helium was then quantitatively cryo-focused on charcoal at ~14 K. Helium was released from the cryo-trap at 34 K and inlet into either a MAP 215-50 (B3-CN-1, B3-CN-3) or GV Helix-SFT (B1-CN-1, B3-CN-4) mass spectrometer. For the MAP 215-50, ^{3}He was analyzed using a channeltron pulse counting electron multiplier, while ^{4}He was analyzed on a faraday cup using magnetic peak-hopping. For the Helix-SFT, ^{3}He and ^{4}He were measured by pulse counting using a Pfeiffer SEM 217 discrete dynode multiplier while using accelerating voltage to hop between masses. Hot blanks were run prior to each analysis (~1300^{o}C) for background corrections and after each analysis (~1350^{o}C) to ensure the sample was completely degassed. Blank corrections constituted between 0.6 to 21% (median = 8.1%) of the total ^{3}He measurements. A standard with a ratio of 2.01 R_A was run frequently during the time of analysis with multiple low He concentration splits analyzed to calibrate pressure non-linearity.

Uncertainties on ^{3}He concentration represent the analytical uncertainty on the measurement coupled with the uncertainty on the blank correction calculated in quadrature. Paleo-exposure times are measured by subtracting the $^{40}Ar/^{39}Ar$ age of the overlying flow from the analyzed flow and propagating the internal uncertainties. The paleo ^{3}He production rate was calculated using the measured ^{3}He concentration and the calculated exposure time. The uncertainty on the paleo production rate includes the age uncertainty associated with the lava flows and the uncertainty on the ^{3}He concentration (2σ).

Results:

One olivine separate from a single hand sample was analyzed from lava flow-top B1, while three separate hand samples were analyzed from flow-top B3. The *in vacuo* crushed olivine separate from B1 contained ^{3}He concentrations that were below detection limit. The detection limit was calculated using three times the standard deviation of the blanks run during the period of analyses (Konrad et al., 2018). The detection limit was 5.4 $x10^{4}$ atoms (2 x 10^{-15} ccSTP) with an average analyzed mass of 0.2 grams resulting in an upper limit concentration of ^{3}He in this sample of 2.7 x 10^{5} atoms/g. The fusion experiment for flow B1 contained 4.49 x 10^{5} atoms/g of ^{3}He (**Table 2**). No crushing experiment was undertaken for flow B3, but numerous other flows from the local sequence contained detection limited (<2.7 x 10^{5} atoms) magmatic ^{3}He concentrations (**Table 1**). Three fusion experiments for flow B3 contained 4.95, 4.31 and 4.14 x 10^{5} atoms/g ^{3}He, resulting in an error-weighted mean concentration of 4.27 x 10^{5} atoms/g. The calculated paleo-production rates for flow-tops B1 and B3 are 56 ± 35 and 39 ± 23 atoms*g^{-1}*a^{-1} respectively (**Table 2**).

Discussion:

Paleo-production rates for ^{3}He

We make the following important assumptions and observations, regarding ^{3}He loss or inheritance in these olivine: (1) Lava flow tops appeared well preserved with no discernable erosional features or paleosol horizons. Additionally, the flows go from a holocrystalline center to a cryptocrystalline, slightly fractured and sometimes glassy flow top with no root casts or evidence of organic material, thus we assume minimal surface erosion between eruption and burial. (2) We assume no post-burial exposure to cosmic rays because overlying flows were a minimum of 4 m in thickness. We assume zero erosion of this overlying flow resulting in a maximum post burial production rate within the 10^{-10} atoms*g^{-1}*s^{-1} range (Lal 1987), which corresponds to a ^{3}He production that corresponds to a maximum of 2.7% (B1) and 2.8% (B3) of our total measured cosmogenic He. (3) That inherited magmatic-derived ^{3}He is negligible given the lack of ^{3}He released during in vacuo crushing of lava flows from this sequence (**Table 1**). (4) Diffusive loss of ^{3}He occurs during likely heating by emplacement of the overlying flows and can be corrected. Our method of crushing samples in ethanol prior to total fusion analyses (Cox et al., 2017; Protin et al., 2016), coupled with detection limited ^{3}He concentrations during crushing analyses imply that all measured ^{3}He is likely cosmogenic with no significant input from inter-crystalline magmatic or atmospheric ^{3}He (**Table 1**).

The uncorrected paleo-production rates of 39 +/- 23 and 56 +/- 35 (2σ) overlap with modern-day values with a probability of 3.3 and 33.1 percent, respectively. These measured paleo-production rates represent minimum values, as ^{3}He is likely diffusively lost when covered by an overlying lava flow.

^{3}He loss due to diffusion

To model diffusive loss of He caused by heating from the overlying flow, we base our boundary conditions on observations of active ocean island lava flows from Kilauea, Hawaii (Hon et al., 1994; Keszthelyi, 1995). These flows are excellent analogues for our Tahitian lava flows because they are similar in size and composition. Keszthelyi (1995) reports that basal temperatures from underneath a molten flow directly after emplacement reach 740^{o}C within one minute. In addition, the temperature within the molten flow increases by 100^{o}C with every two vertical millimeters above the base of the newly emplaced flow (towards the center of the molten flow). We use the maximum temperature and the vertical temperature variations from Keszthelyi (1995) to inform the temperature conditions in the bottom flows of our study pairs from which our cosmogenic nuclide samples were taken. Because the bottom flow is previously crystalline, fully cooled, includes pore water, and the temperatures in molten flows decrease by 50^{o}C per mm from the center of the flow, we conservatively define the maximum temperature for the olivine in the top 4 cm (40 mm) of the underlying flows (from each flow pair) to be between 640^{o}C and 740^{o}C. Certainly, the uppermost few centimeters of the bottom flow must be cooler than the lowermost millimeters of the upper flow. Thus, we use the maximum temperature of the base of the upper flow (740^{o}C) to define a limiting case for the maximum temperature conditions in the underlying flow where we sampled. The Keszthelyi (1995) study did not collect temperatures beyond 20 minutes after lava emplacement. Fortunately, another study reports measurements taken from the surface to 0.1 m depth (within the flow) indicate cooling begins ~1 hr after emplacement, with only the core of the lava flow remaining at maximum temperature for up to 10 hours (Hon et al., 1994). Thus, our diffusion model assumes the underlying flow quickly reaches and then stays at a temperature between 640^{o}C to 740^{o}C for one hour. Then it begins cooling at a rate expressed by

$$T = -354\log(t)+835$$

where T is temperature (°C) and t is hours (Hon et al., 1994). The diffusive loss of He due to heating from the overlying flow was calculated assuming spherical grain geometry using the equations from Crank (1979). A conservative spherical radius of 150 μm was assumed and an E_a of 127 kj/mol and $Ln(D_o)$ of -4.7 cm^2/s (Blard et al., 2008). The model scenario results in a diffusive He loss of 31% (640°C; best estimate) and a firm upper limit of 61% (740°C) from olivine in the underlying flow-top (**Figure 3**).

After correcting for diffusive loss, the new paleo-production rates for olivine from the flow-tops of B1 and B3 are 82 ± 35 and 57 ± 23 atoms*g^{-1}*a^{-1} respectively for a maximum basal temperature of 640°C and 144 ± 35 and 100 ± 23 atoms*g^{-1}*a^{-1} for a maximum basal temperature of 740°C (**Table 3; Figure 3**). Uncertainties include the error on the He measurements and $^{40}Ar/^{39}Ar$ age determinations. These corrected paleo-production rates range from within error of the modern-day production rate (76 ± 12 atoms*g^{-1}*a^{-1}) to the theoretically modeled production rate (124 ± 19 atoms*g^{-1}*a^{-1}) during the time interval when these flow tops were exposed and the paleomagnetic field strength is expected to be low. This suggests the applicability of this method to reconstruct short-lived *in situ* paleo-production rates. The resulting paleo-production rates from the flow tops of B1 and B3 fall within the range of values we can expect even given the large range of temperature values (100°C) we use to correct for the diffusive loss of He. Due to the highly diffusive nature of He and the assumed temperature variations associated with lava emplacement, we cannot report a definitive paleo-production rate for the time interval represented by this sample set. However, we can reasonably rule out scenarios where the production rate increases by more than our upper limit paleo-production rate values (740°C). These values overlap within error with those defined by the PADM2M field strength estimates and LSD scaling factor model (Lifton et al., 2014; Ziegler et al., 2011). While the upper limits of the ^3He modeled production rate (740°C)

agree with the LSD modeled values, the more likely maximum contact temperatures (<700°C) result in production rates lower than the LSD predictions. The diffusion corrected ^{3}He production rates for 640 to 700°C are 82 to 108 atoms*g^{-1}*a^{-1} (B1) and 57 to 75 atoms*g^{-1}*a^{-1} (B3). While we acknowledge the considerable uncertainty on our paleo-production rates given diffusion corrections and ^{40}Ar/^{39}Ar age errors, they are the only observations yet available for this important polarity transition and they suggest that the LSD model may overestimate production rate changes during major paleomagnetic field strength excursions. The potential overestimation may be due to difficulties in quantifying the effects of local non-dipole field components and a possible overestimation of the dipole field strength reduction associated with the M-B precursor event. Additional uncertainties may arise from the use of modern-day atmosphere models (NOAA, 1976; Uppala et al., 2005), which may not accurately represent past atmospheric density.

In this study we have demonstrated that recovering archived cosmogenic nuclide ^{3}He is feasible using sequential lava flow deposits. As the only known method for determining short-lived *in situ* paleo-production rates into deep-time this method has the potential of answering fundamental questions about the behavior of Earth's magnetic field and the role of non-dipole field components in shielding Earth's surface from cosmic rays. Future similar studies should incorporate less diffusive cosmogenic nuclides that are better preserved to accurately define paleo-production rates. ^{21}Ne represents the most studied stable cosmogenic nuclide that is less diffusive than ^{3}He in olivine and pyroxene from basalt flows (Gourbet et al., 2012). The diffusive loss of Ne is estimated to be less than 1% when using the same temperature conditions (640-740°C) applied to the He diffusion model and the activation energy and diffusivity constants from Gourbet et al. (2012). An alternative approach would be to reconstruct a cosmogenic depth profile of ^{3}He in the underlying flow where the shape of the profile would likely deviate from the expected attenuation

profile owing to diffusive loss in a temperature gradient. Alternatively, using rhyolitic lava flows, such as those found in intraplate continental volcanic systems (e.g. Ellis et al., 2013; Manley, 1996) may allow for the use of ^{10}Be and ^{26}Al in quartz phenocrysts. However, both ^{10}Be and ^{26}Al are unstable isotopes and thus their use may be temporally restricted to million-year timescales. The best option would be to analyze two cosmogenic nuclides within a single mineral separate or bulk rock sample to best observe and correct for potential diffusion among the cosmogenic nuclides. This would result in the most robust reconstruction of short-lived cosmogenic nuclide paleo-production rates.

Conclusions:

These measurements represent the first reported short-lived *in situ* paleo-production rates coincident with a paleomagnetic field strength low associated with a polarity reversal. In addition, we report the only known means for reconstructing short-lived paleo-production rates (millennial timescales) that occur hundreds of thousands of years ago. Due to the diffusivity of He in olivine, we are unable to report an absolute ^{3}He paleo-production but have defined the upper limit of *in situ* paleo-production rates during the M-B reversal precursor event. The upper limit (T_{max} = 740ºC) of the diffusion corrected ^{3}He paleo-production rate values are in agreement with the LSD model prediction. However, the more plausible maximum contact temperatures (T_{max}<700ºC) result in corrected ^{3}He paleo-production rates that are lower than predicted. This suggests further investigation is required to better constrain non-dipole field horizontality components, paleo-magnetic field strength and paleo-atmospheric density during this time interval. This supports this method's viability while using a less diffusive element to reconstruct paleo-production rates in volcanic flows with higher K content to reduce age uncertainties. This new method can be used to determine regional short-lived *in situ* paleo-production rates using mineral targets producing ^{21}Ne,

^{10}Be, and/or ^{26}Al cosmogenic nuclides in independently age dated lava flows. Thus, the method can be used to look at paleo-production rate changes associated paleomagnetic anomalies, secular variation, and non-dipole field characteristics. Arguably, constraining this method further using ^{21}Ne would prove most valuable as it can be used to define short-lived paleo-production rate changes into deep-time because it is a stable isotope.

Declaration of interests

☒ The authors declare that they have no known competing financial interests or personal relationships that could have appeared to influence the work reported in this paper.

☐The authors declare the following financial interests/personal relationships which may be considered as potential competing interests:

Acknowledgements

We thank Kevin Konrad for providing the *in vacuo* crushed olivine results and helpful discussions. This work was supported by an NSF AGEP Fellowship for A. Balbas and benefitted greatly from discussions with Peter Clark, Joe Stoner, Brendan Reilly, Ed Brook and Anthony Koppers. We thank two anonymous reviewers for helpful comments that improved the manuscript.

Table 1: Crush-derived Helium isotopic values

Sample	Weight g	Total ^{3}He Released pcc/g	Total ^{4}He Released ncc/g
B1	0.1717	DL	0.42
A2	0.2454	DL	0.60
B5	0.2281	DL	0.44
A7	0.2484	0.02	2.18
A15	0.2037	DL	0.29
A16	0.2593	DL	0.48

DL = 'Detection Limited' defined as three times the standard deviation of the blanks run during time of analyses (2 x 10^{-15} ccSTP), see Konrad et al. (2018) for details.

Table 2: ^{3}He values and exposure ages

Sample	Weight g	Total ^{3}He Released 10^{5} atoms/g	Total ^{3}He Released 10^{5} atoms/g (2σ)	^{40}Ar/^{39}Ar age difference years	^{40}Ar/^{39}Ar uncertainty years (2σ)	Production Rate atoms*g^{-1}*a^{-1}	Production Rate atoms*g^{-1}*a^{-1} (2σ)
B1-CN-1	0.723	4.49	0.33	8000	5022	56	35
B3-CN-1	0.316	4.95	0.77	10900	6185	45	27
B3-CN-3	0.302	4.14	0.38			38	22
B3-CN-4	0.984	4.31	0.29			40	23
B3-Total		4.27	0.18			39	23

^{40}Ar/^{39}Ar age determinations from Balbas et al. (2018).

Table 3: ^{3}He Paleo-production Rates

Flow Top	Peak Temperature °C	Production Rate atoms*g^{-1}*a^{-1}	± Production Rate atoms*g^{-1}*a^{-1} (2σ)
B1	-	56	*35*
	640	82	"
	740	144	"
B3	-	39	*23*
	640	57	"
	740	100	"

Peak temperature represents the maximum equilibration temperature with the overlying flow, see text for details.

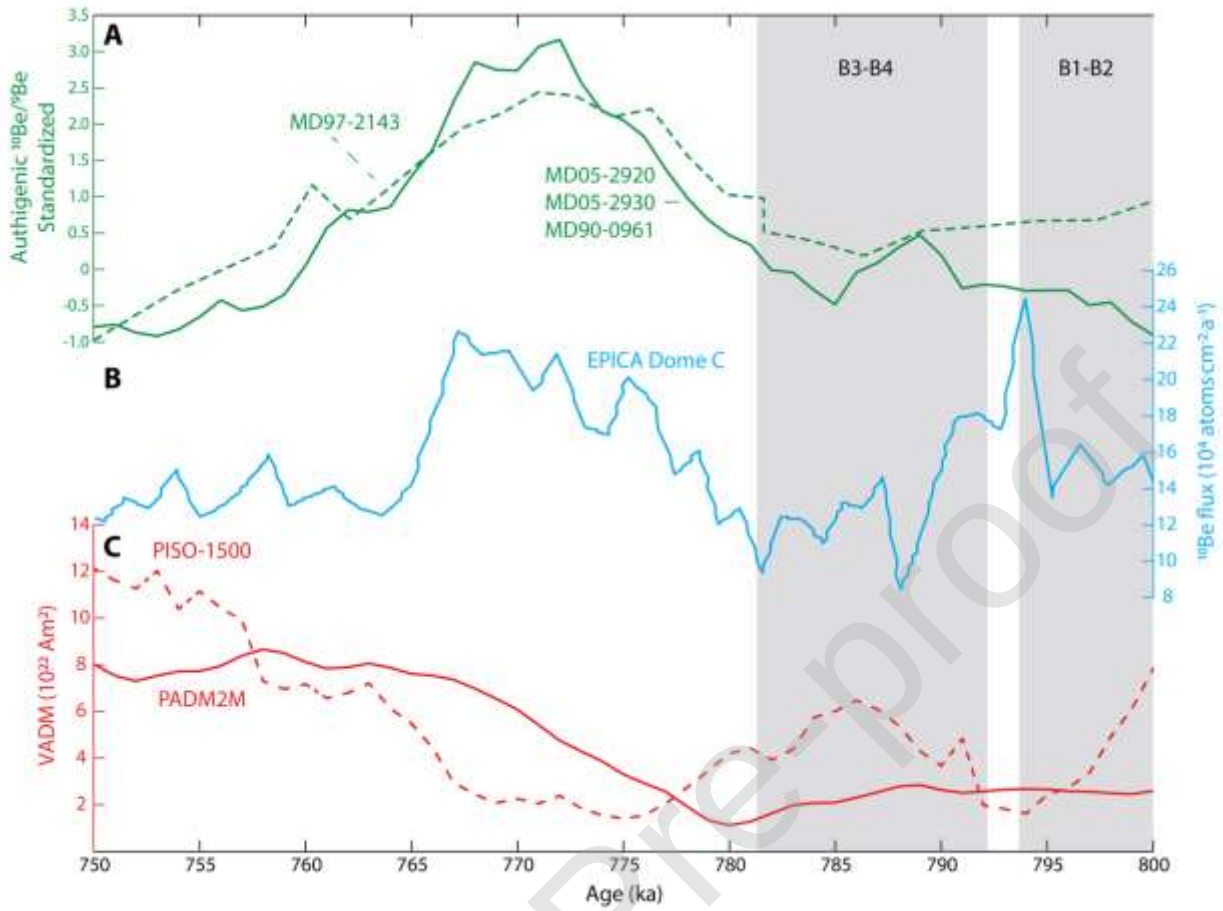

Figure 1: Variations in atmospheric ^{10}Be concentration and paleomagnetic field intensity through the Matuyama-Bruhnes reversal and precursor event. (A) Standardized ^{10}Be/^{9}Be record from marine sediment cores MD97-2143 (dashed line) and stacked MD05-2920, MD05-2930 and MD90-0961 (solid line) (Simon et al., 2018a; Simon et al., 2018b). (B) ^{10}Be flux recorded in an ice core from EPICA Dome C (Raisbeck et al., 2006) on the age model AICC2012 (Bazin et al., 2013). (c) Virtual axial dipole moment (VADM) through time determined from stacked sedimentary core records (PISO-1500, Channell et al., 2009) and stacked sedimentary/lava flow records (PADM2M, Ziegler et al., 2011). The exposure durations for flows B1 and B3 are shown with grey shading.

Figure 2: The contact between lava flows B3 and B4. The yellow chalk line represents the contact between the rubbly top of B3 and the solid base of B4. Samples B3-CN were taken from below the yellow chalk line. A yellow notebook is shown for a scale with a length of ~12.7 cm.

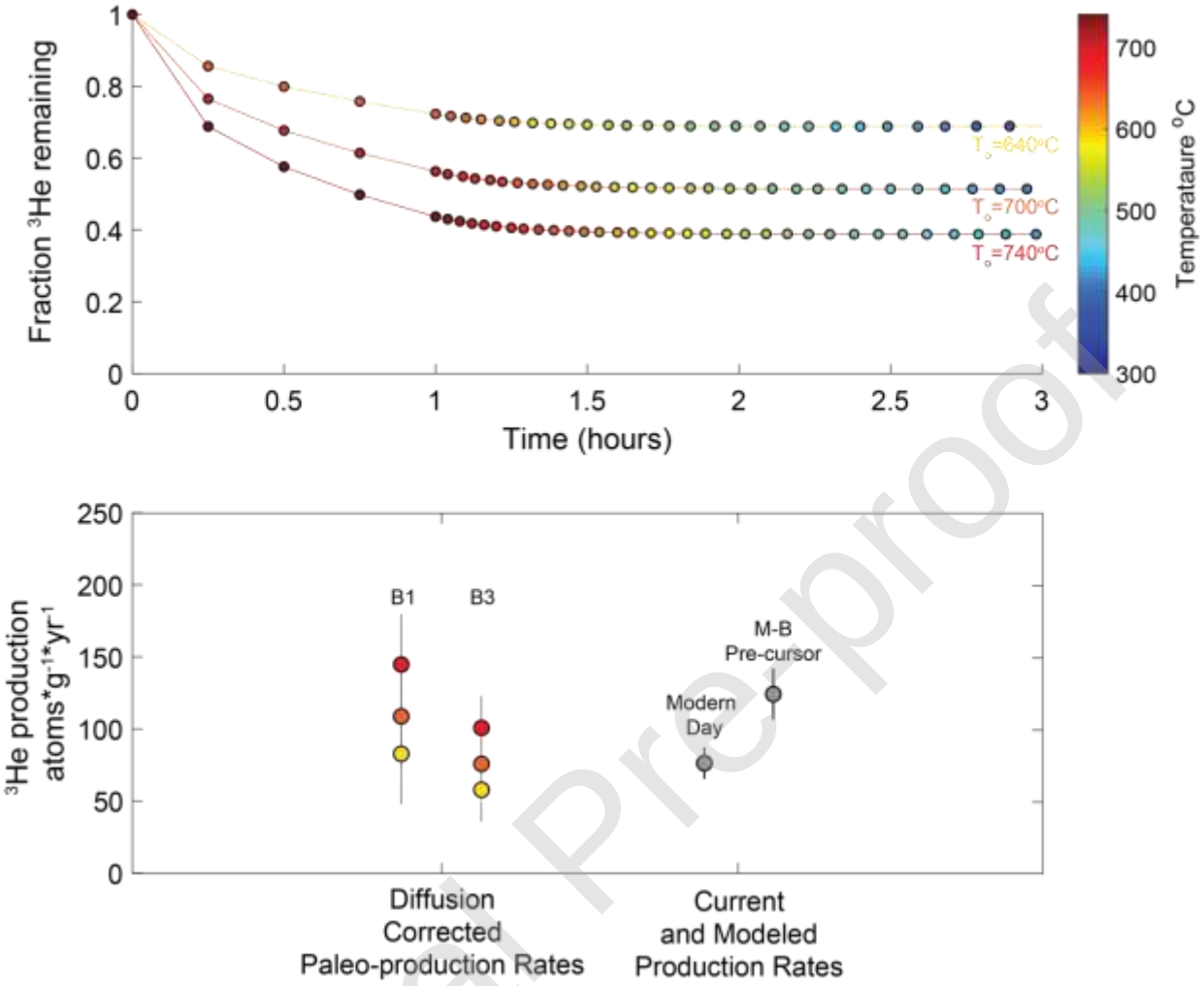

Figure 3: Modeled He diffusion in olivine and corresponding paleo-production rates after diffusive loss corrections. (A) Models of He diffusion in olivine using the temperatures and cooling rates discussed in the text. The model uses a Ln(D_o) of -4.7 cm^2/s and an Ea of 127 kJ/mol for olivine (Blard et al., 2008). The diffusion model conservatively assumes spherical grain sizes at a radius of 150 µm. (B) Calculated paleo-production rates for ^{3}He corrected using diffusion results from (A). The modern day and M-B precursor production rates and corresponding error for the field site are shown as grey circles and calculated using the Goehring et al. (2010) production rate, scaled using the LSD model (Lifton et al., 2014). The production rate uncertainties include the coupled ^{3}He and ^{40}Ar/^{39}Ar uncertainties shown with 2σ confidence. The modeled corrected production rate uncertainties do not include the error on Ea and Ln(Do).

References:

Balbas, A. et al., 2018. Millennial-Scale Instability in the Geomagnetic Field Prior to the Matuyama-Brunhes Reversal. Geochemistry, Geophysics, Geosystems, 19(3): 952-967.

Bazin, L. et al., 2013. An optimized multi-proxy, multi-site Antarctic ice and gas orbital chronology (AICC2012): 120-800 ka. Climate of the Past, 9(4): 1715.

Blard, P.-H., Puchol, N., Farley, K., 2008. Constraints on the loss of matrix-sited helium during vacuum crushing of mafic phenocrysts. Geochimica et Cosmochimica Acta, 72(15): 3788-3803.

Channell, J., Xuan, C., Hodell, D., 2009. Stacking paleointensity and oxygen isotope data for the last 1.5 Myr (PISO-1500). Earth and Planetary Science Letters, 283(1): 14-23.

Coe, R.S., Glen, J.M., 2004. The complexity of reversals. Timescales of the Paleomagnetic Field: 221-232.

Cox, S., Miller, H., Farley, K., Hofmann, F., 2017. Anomalous trapping of noble gases during sample crushing, AGU Fall Meeting Abstracts.

Crank, J., 1979. The mathematics of diffusion. Oxford university press.

Desilets, D., Zreda, M., & Prabu, T. (2006). Extended scaling factors for in situ cosmogenic nuclides: new measurements at low latitude. Earth and Planetary Science Letters, 246(3-4), 265-276.

Ellis, B. et al., 2013. Rhyolitic volcanism of the central Snake River Plain: a review. Journal of Quaternary Science, 75(8): 745.

Elsasser, W., Ney, E., Winckler, J., 1956. Cosmic-ray intensity and geomagnetism. Nature, 178(4544): 1226.

Fadil, A., Sichoix, L., Barriot, J. P., Ortega, P., & Willis, P. (2011). Evidence for a slow subsidence of the Tahiti Island from GPS, DORIS, and combined satellite altimetry and tide gauge sea level records. Comptes Rendus Geoscience, *343*(5), 331-341.

Goehring, B.M. et al., 2010. A reevaluation of in situ cosmogenic 3He production rates. Quaternary Geochronology, 5(4): 410-418.

Gosse, J.C., Phillips, F.M., 2001. Terrestrial in situ cosmogenic nuclides: theory and application. Quaternary Science Reviews, 20(14): 1475-1560.

Gourbet, L. et al., 2012. Neon diffusion kinetics in olivine, pyroxene and feldspar: retentivity of cosmogenic and nucleogenic neon. Geochimica et Cosmochimica Acta, 86: 21-36.

Gubbins, D., 1999. The distinction between geomagnetic excursions and reversals. Geophysical Journal International, 137(1): F1-F3.

Hartl, P., Tauxe, L., 1996. A precursor to the Matuyama/Brunhes transition-field instability as recorded in pelagic sediments. Earth and Planetary Science Letters, 138(1): 121-135.

Hon, K., Kauahikaua, J., Denlinger, R., Mackay, K., 1994. Emplacement and inflation of pahoehoe sheet flows: Observations and measurements of active lava flows on Kilauea Volcano, Hawaii. Geological Society of America Bulletin, 106(3): 351-370.

Jarboe, N.A., Coe, R.S., Glen, J.M.G., 2011. Evidence from lava flows for complex polarity transitions: the new composite Steens Mountain reversal record. Geophysical Journal International, 186(2): 580-602.

Keszthelyi, L., 1995. Measurements of the cooling at the base of pahoehoe flows. Geophysical Research Letters, 22(16): 2195-2198.

Konrad, K., Graham, D.W., Kent, A.J., Koppers, A.A., 2018. Spatial and temporal variability in Marquesas Islands volcanism revealed by 3 He/4 He and the composition of olivine-hosted melt inclusions. Chemical Geology, 477: 161-176.

Kurz, M.D., 1986. In situ production of terrestrial cosmogenic helium and some applications to geochronology. Geochimica et Cosmochimica Acta, 50(12): 2855-2862.

Lal, D. (1987). Production of 3He in terrestrial rocks. Chemical Geology: Isotope Geoscience Section, 66(1-2), 89-98.

Leduc, G., Thouveny, N., Bourlès, D., Blanchet, C., Carcaillet, J., 2006. Authigenic 10Be/9Be signature of the Laschamp excursion: a tool for global synchronisation of paleoclimatic archives. Earth and Planetary Science Letters, 245(1-2): 19-28.

Lifton, N., Sato, T., Dunai, T.J., 2014. Scaling in situ cosmogenic nuclide production rates using analytical approximations to atmospheric cosmic-ray fluxes. Earth and Planetary Science Letters, 386: 149-160.

Manley, C.R., 1996. Morphology and maturation of melt inclusions in quartz phenocrysts from the Badlands rhyolite lava flow, southwestern Idaho. American Mineralogist, 81(1-2): 158-168.

McElhinny, M., McFadden, P.L., 1998. The magnetic field of the earth: paleomagnetism, the core, and the deep mantle, 63. Academic Press.

McFadden, P., Merrill, R., McElhinny, M., Lee, S., 1991. Reversals of the Earth's magnetic field and temporal variations of the dynamo families. Journal of Geophysical Research: Solid Earth (1978–2012), 96(B3): 3923-3933.

McHargue, L.R., Damon, P.E., Donahue, D.J., 1995. Enhanced cosmic-ray production of 10Be coincident with the Mono Lake and Laschamp Geomagnetic Excursions. Geophysical Research Letters, 22(5): 659-662.

Mead, G.D., 1964. Deformation of the geomagnetic field by the solar wind. Journal of Geophysical Research, 69(7): 1181-1195.

Menabreaz, L., Bourles, D.L., Thouveny, N., 2012. Amplitude and timing of the Laschamp geomagnetic dipole low from the global atmospheric 10Be overproduction: contribution of authigenic 10Be/9Be ratios in west equatorial Pacific sediments. Journal of Geophysical Research: Solid Earth, 117(B11): 2156-2202.

Ménabréaz, L. et al., 2011. The Laschamp geomagnetic dipole low expressed as a cosmogenic 10 Be atmospheric overproduction at~ 41ka. Earth and Planetary Science Letters, 312(3): 305-317.

Mochizuki, N., Oda, H., Ishizuka, O., Yamazaki, T., Tsunakawa, H., 2011. Paleointensity variation across the Matuyama-Brunhes polarity transition: Observations from lavas at Punaruu Valley, Tahiti. Journal of Geophysical Research: Solid Earth (1978–2012), 116(B6).

Muscheler, R., Beer, J., Kubik, P.W., Synal, H.A., 2005. Geomagnetic field intensity during the last 60,000 years based on 10Be and 36Cl from the Summit ice cores and 14C. Quaternary Science Reviews, 24(16-17): 1849-1860.

NOAA, 1976. US standard atmosphere. US Goverment Printing Office.

Pillans, B., 1997. Soil development at snail's pace: evidence from a 6 Ma soil chronosequence on basalt in north Queensland, Australia. Geoderma, 80(1-2): 117-128.

Protin, M., Blard, P.-H., Marrocchi, Y., Mathon, F., 2016. Irreversible adsorption of atmospheric helium on olivine: A lobster pot analogy. Geochimica et Cosmochimica Acta, 179: 76-88.

Raisbeck, G., Yiou, F., Cattani, O., Jouzel, J., 2006. 10Be evidence for the Matuyama–Brunhes geomagnetic reversal in the EPICA Dome C ice core. Nature, 444(7115): 82-84.

Raisbeck, G. et al., 1981. Cosmogenic 10Be concentrations in Antarctic ice during the past 30,000 years. Nature, 292(5826): 825.

Simon, Q. et al., 2017. Authigenic 10Be/9Be ratio signature of the Matuyama–Brunhes boundary in the Montalbano Jonico marine succession. Earth and Planetary Science Letters, 460: 255-267.

Simon, Q. et al., 2018a. Cosmogenic signature of geomagnetic reversals and excursions from the Réunion event to the Matuyama–Brunhes transition (0.7–2.14 Ma interval). Earth and Planetary Science Letters, 482: 510-524.

Simon, Q. et al., 2018b. Increased production of cosmogenic 10 Be recorded in oceanic sediment sequences: Information on the age, duration, and amplitude of the geomagnetic dipole moment minimum over the Matuyama–Brunhes transition. Earth and Planetary Science Letters, 489: 191-202.

Singer, B.S. et al., 2005. Structural and temporal requirements for geomagnetic field reversal deduced from lava flows. Nature, 434(7033): 633-6.

Suganuma, Y. et al., 2010. 10Be evidence for delayed acquisition of remanent magnetization in marine sediments: Implication for a new age for the Matuyama–Brunhes boundary. Earth and Planetary Science Letters, 296(3): 443-450.

Thébault, E. et al., 2015. International geomagnetic reference field: the 12th generation. Earth, Planets and Space, 67(1): 79.

Uppala, S.M. et al., 2005. The ERA-40 re-analysis. Quarterly Journal of the Royal Meteorological Society: A journal of the atmospheric sciences, applied meteorology physical oceanography, 131(612): 2961-3012.

Valet, J.-P., Plenier, G., 2008. Simulations of a time-varying non-dipole field during geomagnetic reversals and excursions. Physics of the Earth and Planetary Interiors, 169(1): 178-193.

Ziegler, L., Constable, C., Johnson, C., Tauxe, L., 2011. PADM2M: a penalized maximum likelihood model of the 0–2 Ma palaeomagnetic axial dipole moment. Geophysical Journal International, 184(3): 1069-1089.